Computers, Materials & Continua CMC, vol.62, no.3, pp.1201-1215, 2020

Automatic Detection of Aortic Dissection Based on Morphology and Deep Learning

Yun Tan[1, #], Ling Tan[2, #], Xuyu Xiang[1, *], Hao Tang[2, *], Jiaohua Qin[1] and Wenyan Pan[1]

Abstract: Aortic dissection (AD) is a kind of acute and rapidly progressing cardiovascular disease. In this work, we build a CTA image library with 88 CT cases, 43 cases of aortic dissection and 45 cases of health. An aortic dissection detection method based on CTA images is proposed. ROI is extracted based on binarization and morphology opening operation. The deep learning networks (InceptionV3, ResNet50, and DenseNet) are applied after the preprocessing of the datasets. Recall, F1-score, Matthews correlation coefficient (MCC) and other performance indexes are investigated. It is shown that the deep learning methods have much better performance than the traditional method. And among those deep learning methods, DenseNet121 can exceed other networks such as ResNet50 and InceptionV3.

Keywords: Aortic dissection detection, morphology, DenseNet.

1 Introduction

Aortic dissection (AD) is a kind of dangerous cardiovascular disease with rapid onset, rapid progress and high clinical mortality rate. It originates from the intimal tears formed by the intima and medial layers of the aortic wall. Driven by the aortic pressure, the blood in the aortic directly penetrates the middle layer of the aortic through the intimal tear, resulting in the formation of middle layer separation. With the change of disease spectrum, the incidence of aortic dissection is increasing year by year.

Multi-slice CT angiography (CTA) is a non-invasive angiographic technique based on multi-slice spiral CT scanning imaging, which aims at displaying blood vessels in different parts of the body by injecting a contrast agent into blood vessels. It can not only provide morphological information on lumen changes, but also can show pathological conditions for wall lesions. It has the advantages of the fast, accurate, non-invasive, safe, repeatable, wide field of vision, high temporal and spatial resolution. At the same time, there are multiple reconstruction methods and post-processing functions available.

[1] College of Computer Science and Information Technology, Central South University of Forestry & Technology, Changsha, 410114, China.

[2] The Second Xiangya Hospital of Central South University, Changsha, 410011, China.

[*] Corresponding Authors: Xuyu Xiang. Email: xyuxiang@163.com;

Hao Tang. Email: dr.tanghao@csu.edu.cn.

[#] The authors contributed equally to this work.

Therefore, CTA has been widely used for the diagnosis of aortic dissection and is currently the preferred method of examination for aortic dissection diagnosis and follow-up. However, since the aortic dissection usually has a large range of lesions, each patient will have 300-500 CTA images. The analysis of the aortic CTA images and the release of the final report need to spend several hours for a radiologist with many years of experience. At the same time, since the manual reading is based on the doctor's personal experience, the accuracy is difficult to be quantified and ensured. And misdiagnosis and missed diagnosis are easily caused by a doctor's mistake and fatigue.

In recent years, the medical image-assisted diagnosis has become one of the most popular directions in the field of artificial intelligence medical treatment. Traditional machine learning methods cannot effectively mine the rich information contained in medical images. However, deep learning builds hierarchical models by simulating the human brain. It has the powerful ability of automatic feature extraction and complex model construction with high efficiency. It can express features and extract features from the bottom to the top level from the raw data of the pixel level, providing a new way to solve the new problems faced by medical image recognition. Therefore, deep learning methods, especially convolutional neural networks (CNN), has become a hot spot in medical image analysis. Kooi et al. used CNN for the identification of malignant lesions in the breast, which resulted in a more accurate recognition rate than traditional computer-aided methods [Kooi, Litjens, Van et al. (2017)]. Grinsven et al. proposed an improved CNN model for detecting bleeding lesions in color fundus images [Grinsven, Ginneken, Hoyng et al. (2016)]. Dou et al. used 3D CNN to extract more representative advanced features from MRI images, thus enabled automatic detection of brain microbleeds with detection accuracy above 90% [Dou, Chen, Yu et al. (2016)]. Sirinukunwattana et al. used spatially constrained convolutional neural networks (SC-CNN) to detect and classify colorectal adenocarcinoma cells, and used proximity integrated prediction methods to obtain better classification effects than classical feature classification methods [Sirinukunwattana, Raza, Tsang et al. (2016)]. Zreik et al. proposed a CTA-based diagnosis of coronary artery stenosis, which can achieve higher specificity [Zreik, Lessmann, Hamersvelt et al. (2018)].

However, the research of automatic detection of aortic dissection is still relatively racking. Gayhart et al. built an automatic detection method for aortic dissection and penetrating aortic ulcer (PAU) based on contrast-enhanced CT Scan, which is mainly based on the analysis of shape characteristics of the aortic artery and aortic arch. It can achieve a sensitivity of 0.8218 and a specificity of 0.9907 for aortic dissection detection. But it was only applied to 9 cases of CT data. At the same time, the shapes of the aortic artery and aortic arch are deformed due to the variation of scanning angle in some CT cases, which may lead to wrong judgement [Gayhart and Arisawa (2013)]. Zheng et al. used General Hough Transform (GHT) to detect the shape of the aorta and used K-means clustering to position the aorta initially. Bayesian tracking method was applied to track the aorta vessel. This method was verified on 24 CT datasets and shew encouraging performance. But this paper only focused on the aorta detection and the detection of aortic dissection was not involved [Zheng, Carr and Ge (2013)]. Dehghan et al. proposed an automatic detection method of aortic dissection based on segmentation refinement, flap detection and shape analysis, which was tested on a data set of 37 contrast-enhanced CT volumes. The results show an accuracy of 83.8%, a sensitivity of 84.6% and a specificity of 83.3% [Dehghan,

Wang, Syeda-Mahmood et al. (2017)]. It can be seen that the current automatic detection methods for aortic dissection are mainly based on traditional image analysis methods. The deep learning based methods have not yet been popularized.

The main contributions of this work are as follows: firstly, we build a CTA image dataset with 88 CTA cases including 43 cases of aortic dissection and 45 cases of health. All these images come from the clinical data of the department of cardiovascular surgery in the Second Xiangya Hospital of Central South University in China. Two experienced cardiovascular experts are responsible for making label for the two class of the images: aortic dissection or normal. Secondly, we propose an aortic dissection detection method based on CTA images. The deep learning models were applied to the region of interests (ROI) of the datasets. Finally, we apply our method to the 88 CTA cases, which includes 4840 slice images. The accuracy and sensitivity were investigated and compared between traditional image analysis methods and deep learning methods, which includes DenseNet, Resnet, and InceptionV3.

The paper is organized as follows: Relevant medical background is introduced in Section 2, and the proposed method is introduced in Section 3. Experimental results and comparisons are shown in Section 4. Finally, we conclude this paper in Section 5.

2 Relevant background

2.1 Aortic dissection detection basis

Aortic dissection refers to the fact that blood in the aortic cavity enters the aortic media through the intimal tear of aortic intima, which separates the middle layer and extends along the long axis of the aorta to form a true and false lumen of the aortic wall. Fig. 1 shows CTA images of a patient with aortic dissection. With the change of scanning position, the shape of the aorta also changes in CTA images. Fig. 1(a) shows dissection of the aortic arch and the yellow rounded part is the region of the aortic arch. Fig. 1(b) shows dissection of ascending and descending aorta, and the two yellow rounded parts are the regions of ascending and descending aorta separately. The main basis of our judgment is that interlayer appears in the yellow parts of the CTA images.

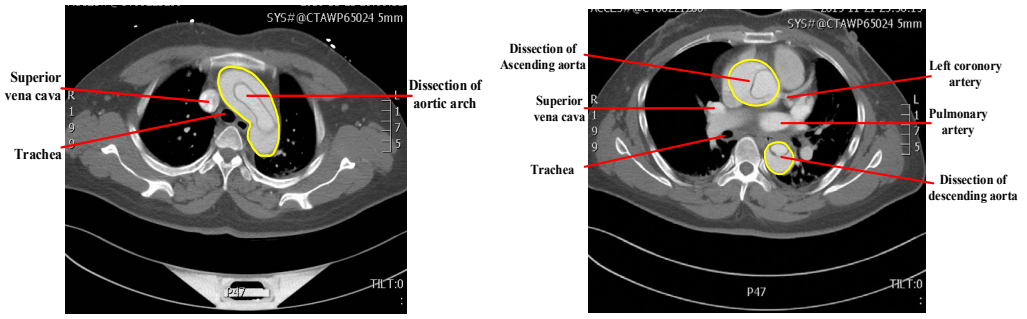

(a) (b)

Figure 1: CTA images of aortic dissection: (a) Dissection of aortic arch (b) Dissection of ascending and descending aorta

2.2 Dataset establishment

We collected CTA images from the clinical data of the department of cardiovascular surgery in the Second Xiangya Hospital of Central South University in China. With the consideration of morphological difference of aorta in different locations, such as aortic arch, ascending and descending aorta, the CTA images datasets are organized as 4 classes as shown in Tab. 1. There are 4840 slice images coming from 88 CTA cases, which includes 43 cases of aortic dissection and 45 normal cases. The number and proportion of each class are also listed in Tab. 1.

Table 1: Dataset organization

Class type	Description	Sample	Number	Proportion
Class 0	Normal aortic arch		709	14.65%
Class 1	Normal ascending and descending arch	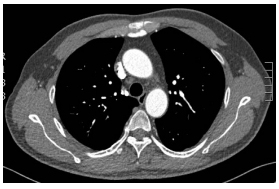	1763	36.42%
Class 2	Aortic arch with aortic dissection		629	13.00%
Class 3	Ascending and descending arch with aortic dissection		1739	35.93%

2.3 OSTU binarization

The OSTU method [Otsu (1979)] is classical for the threshold selection in image binarization. It can achieve the optimal threshold by maximizing the separability of the resultant classes in gray levels.

Assuming M_0 and M_1 are the foreground part and background part of the image separately. The probabilities of their occurrence are:

$$\xi_0 = \Pr(M_0) = \sum_{i=1}^{k} p_i = \xi(k) \tag{1}$$

$$\xi_1 = \Pr(M_1) = \sum_{i=k+1}^{L} p_i = 1 - \xi(k) \tag{2}$$

where L is the total gray levels of the image. Then the class mean levels can be represented as:

$$\mu_0 = \sum_{i=1}^{k} i \Pr(i|M_0) = \sum_{i=1}^{k} \frac{ip_i}{\xi_0} = \frac{\mu(k)}{\xi(k)} \tag{3}$$

$$\mu_1 = \sum_{i=k+1}^{L} i \Pr(i|M_1) = \sum_{i=k+1}^{L} \frac{ip_i}{\xi_1} = \frac{\mu(L) - \mu(k)}{1 - \xi(k)} \tag{4}$$

The class variances can be given by:

$$\sigma_0^2 = \sum_{i=1}^{k} (i - \mu_0)^2 \Pr(i|M_0) = \sum_{i=1}^{k} \frac{(i - \mu_0)^2 p_i}{\xi_0} \tag{5}$$

$$\sigma_1^2 = \sum_{i=k+1}^{L} (i - \mu_1)^2 \Pr(i|M_1) = \sum_{i=k+1}^{L} \frac{(i - \mu_1)^2 p_i}{\xi_1} \tag{6}$$

$$\sigma_B^2(k) = \frac{[\mu(L)\xi(k) - \mu(k)]^2}{\xi(k)[1 - \xi(k)]} \tag{7}$$

By maximizing the $\sigma_B^2(k)$, the optimal threshold can be achieved.

3 Proposed method

Our proposed method includes two main parts: ROI (Region of Interest) extraction and deep learning based detection, as shown in Fig. 2.

3.1 ROI extraction

For CTA images, the middle aorta part is the most important that need to be paid attention to, and it is also the main basis for aortic dissection. In order to reduce the impact of unrelated areas on diagnosis, we need to perform ROI extraction firstly.

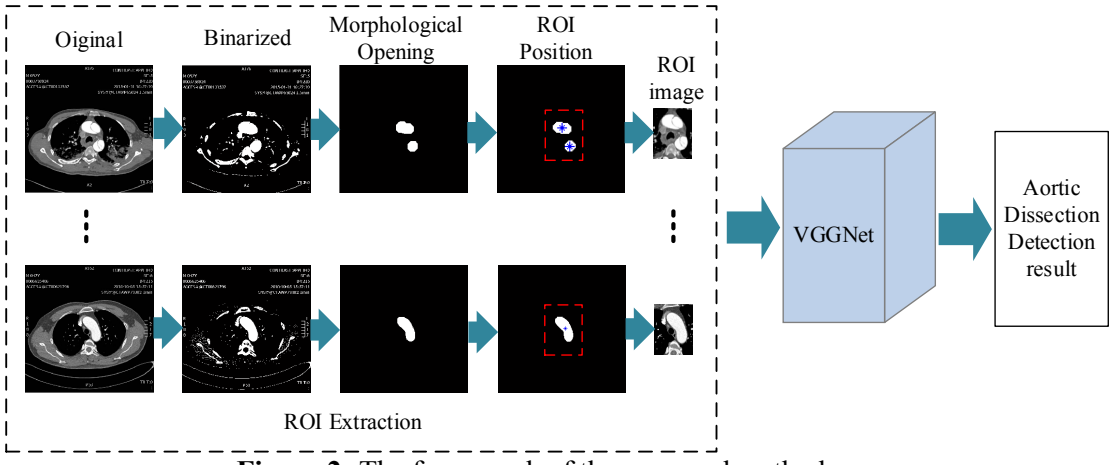

Figure 2: The framework of the proposed method

3.1.1 Binarization

A complete CTA image can be divided into two parts: the information area and the abdominal area. The information area usually includes the private information of the patient and the device information for CTA scanning, which has large area black background and will not affect detection. While in the abdominal area, the middle aortic portion usually exhibits a significantly larger grayscale due to the influence of the contrast agent. Therefore, binarization is used to divide the CTA image into foreground and background image. At the same time, the image part of the abdominal cavity is expected to be separated from the aorta as much as possible by binarization.

However, sometimes the grayscale value of the abdominal cavity is similar to the aorta due to the insufficient contrast injection as shown in Fig. 3(a). It is difficult to extract the aorta part and exclude abdominal cavity part successfully. In fact, the abdominal cavity will be classified as foreground with the high possibility with the normal OSTU method, as shown in Fig. 3(b). During the image processing field, the adaptive threshold is usually used to adapt to the variety of image features [Li, Qin, Xiang et al. (2018)]. The adaptive OSTU binarization method was proposed and shew improvements of binarization results with the restoration of weak connections [Moghaddam and Cheriet (2010)]. Adaptive image contrast was also used for image binarization and achieve text recovery finally [Ingle and Kaur (2017)]. However, most of the current adaptive binarization methods mainly focus on restoration of degraded images. While during CTA images processing, our target is to extend the intra-variation and separate aorta part from the abdominal cavity part successfully. Therefore, a blocking OSTU method is proposed. As shown in Fig. 3(c), the original image is divided to 8×8 subblocks. The OSTU threshold is calculated based on every subblock separately. We choose the maximum value of the sub-block thresholds as the final threshold of binarization and the achieved binary image is shown as Fig. 3(d).

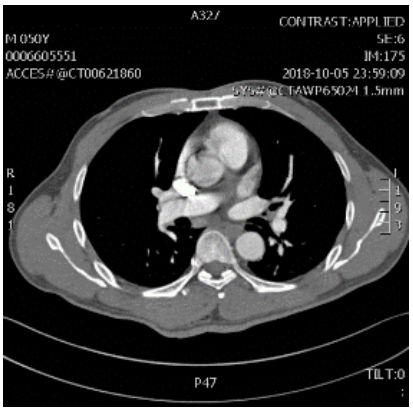

(a)

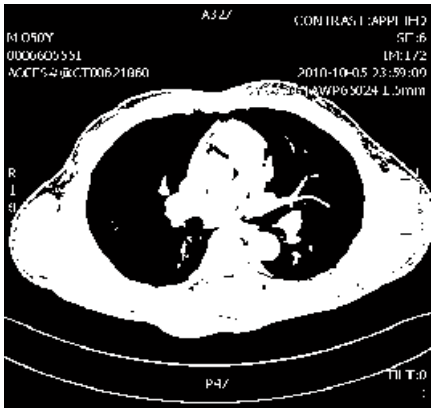

(b)

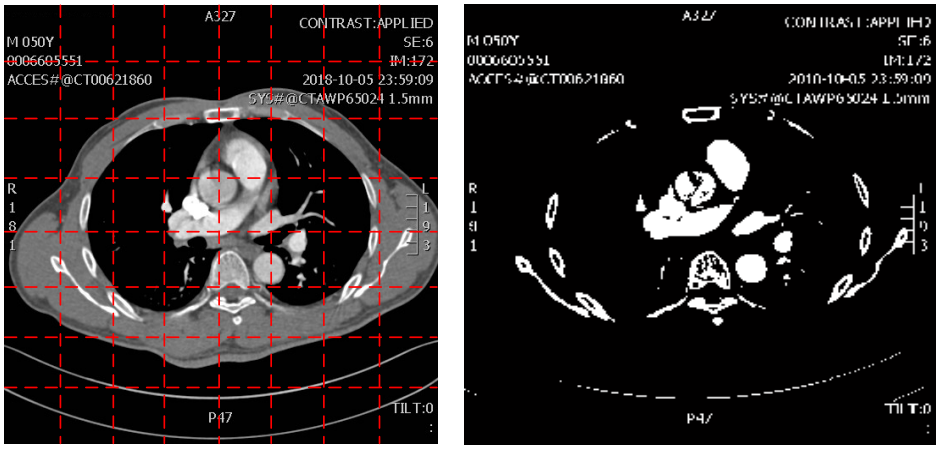

(c) **(d)**

Figure 3: CTA images: (a)Original image with insufficient contrast injection (b) Binary image with normal OSTU threshold (c) Image divided to 8x8 subblock (d) Binary image with blocking OSTU threshold

The blocking OSTU algorithm is described in Algorithm 1.

Algorithm 1: Binarization based on blocking OSTU

Input: original gray CTA image M
Output: binary image B
1: Divide M to 8×8 subblocks M_1~M_64
2: Calculate OSTU threshold for every subblock:
3: for i=1:64
4: Thres(i)=OSTU_thres(M_i)
5: End
6: Threshold=max(Thres(i))
7: Achieve binary image B:
8: for i=size(M)
9: if M_pixel(i) > Threshold
10: B_pixel(i)=1
11: else
12: B_pixel(i)=0
13: end
14: end

3.1.2 Opening operation

For the binary image, there are some noise spots and the interference of abdominal cavity still exists. We use the mathematical morphology opening operation as the next step to remove these effects.

In mathematical morphology, usually, a set of transformations are used to describe the basic features or basic structure of an image. The most basic transformations are corrosion and expansion [Najman and Talbot (2013)]. Corrosion will reduce the range of the target area, which will cause the edge of the image to shrink in essence, and can be used to eliminate small and meaningless objects. It can be expressed as

$$A \ominus B = \{x, y \left| (B)_{xy} \subseteq A \right.\} \tag{8}$$

where A is the original image and B is the structural element that used to corrode A.

The expansion will merge the background points contacted with the target area into the target object, which will expand the target boundary to the outside and enlarge the range of the target area. It can be used to fill some holes in the target area and eliminate the small particle noise contained in the target area. It can be expressed as:

$$A \oplus B = \{x, y \left| (B)_{xy} \cap A \neq \varnothing \right.\} \tag{9}$$

where A is the original image and B is the structure element that used to expand A.

The opening operation is defined as the operation of expansion after corrosion, which can be represented as follows:

$$A \circ B = (A \ominus B) \oplus B \tag{10}$$

where A is the original image and B is the structural element that used to transform A. Through opening operation, the isolated small dots and burrs that are smaller than the structural elements are removed. And the bridges and elongated laps are cut off to separate. At the same time, overall position and shape are unchanged.

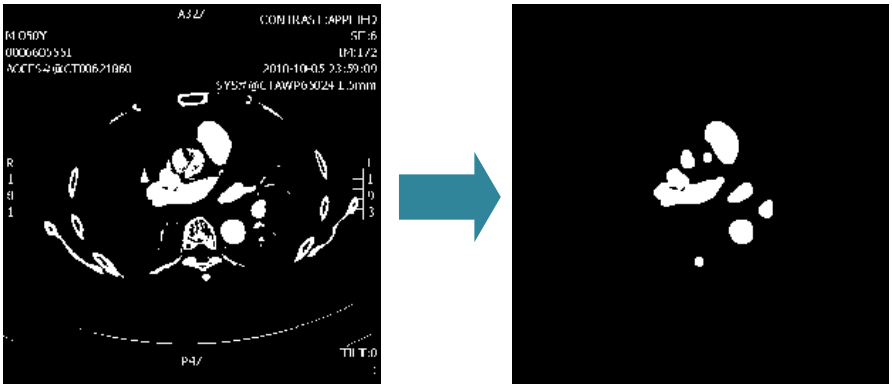

Before Opening Operation

After Opening Operation

Figure 4: Effect of opening operation

As shown in Fig. 4, after the opening operation, the part of the abdominal cavity has been completely removed from the binary image.

3.1.2 ROI positioning

In order to position the ROI actually, the area of connected components is calculated. If the area is smaller than a *thres*_n, it will be removed as noise spot. Then remained connected parts are considered as our interested parts.

The centroid of every interested part is calculated. There are possibly more than one centroids. Therefore, assuming $x(i)$ and $y(i)$ are the row and column positions of the ith centroid, then we calculate the center of the ROI as follows:

$$x\_\mathrm{c} = \frac{\max\left(x(i)\right) + \min\left(x(i)\right)}{2} \tag{11}$$

$$y\_\mathrm{c} = \frac{\max\left(y(i)\right) + \min\left(y(i)\right)}{2} \tag{12}$$

where $1 \le i \le L$ (L is the number of connected components remained), x_c and y_c are the row and column position of the ROI center separately. Then the ROI is extracted from the original CTA image, as shown in Fig. 5.

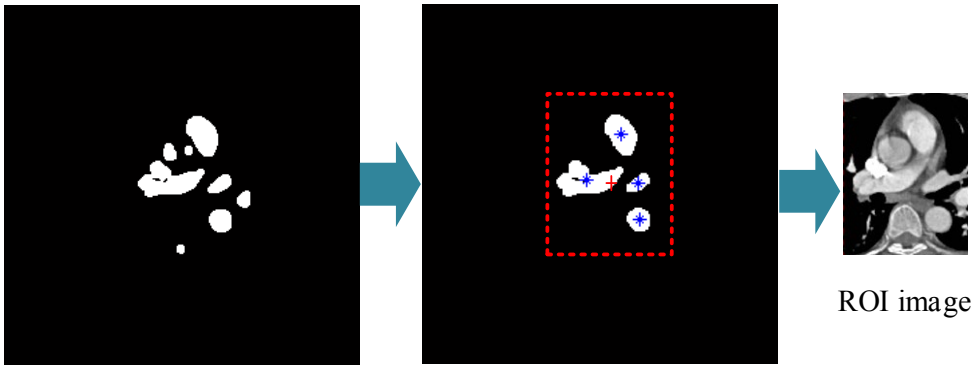

Figure 5: Positioning of ROI

During the processing, there are some non-aortic components that are always present, such as superior vena cava and coronary artery, it is difficult to discriminate them from aorta using morphology methods since they have similar shapes and greyscale. But the ROI extraction still shows complete part of the aorta. We keep the accurate detect task to deep learning model in the next step.

3.2 Detection based on DenseNet

Since 2014, the performance of CNN has been improved greatly by using deeper and wider network structure. The Inception module was proposed [Szegedy, Liu, Jia et al. (2015)], which achieved the performance improvement of the network by using multiple convolutional kernels with different sizes. But this structure led to a large number of

module parameters. Later the InceptionV2 and IncepionV3 were proposed to further optimize the network performance [Szegedy, Vanhoucke, Ioffe et al. (2016)]. In the InceptionV2, two 3×3 convolution kernels instead of 5×5 convolution were used to reduce the number of parameters and establish more non-linear transformations, which strengthened the learning capability of CNN. At the same time, batch normalization (BN) was proposed for data regularization and speeded up the network training process. While in the InceptionV3, the idea of factorization into small convolutions was further utilized and reduced the phenomenon of over-fitting.

In another hand, the increment of neural networks depth also increases the difficulty of network training. At the same time, traditional convolutional networks or fully connected networks will lose information more or less when transmitting information. Gradient disappearance or gradient explosion will also lead to the problem that deep networks cannot be trained successfully. Therefore, the idea of residual learning (ResNet) was put forward in 2015 [He, Zhang, Ren et al. (2015)], which solved this problem to a certain extent. By directly transferring input information to output through a bypass, the integrity of information was protected. The whole network only needs to learn the difference between input and output, which can simplify the learning goal and difficulty.

While during the research of ResNet, it was found that that dropping some layers randomly at each step of the training process could significantly improve the generalization performance of ResNet. It means that the neural network is not necessarily a progressive hierarchical structure. A layer in the network may depend not only on the characteristics of the adjacent upper layer, but also on the characteristics of the earlier layer. In fact, removing several layers of the trained ResNet randomly would not impact the network prediction results greatly, which shows that ResNet has some redundancy, and only a few features are extracted from each layer of the network. Therefore, Densely connected convolutional network (DenseNet) was proposed by Huang et al. [Huang, Liu, Maaten et al. (2017)]. It connects every layer to all the other layers as a feed-forward, which increases direct connections to $L(L+2)/2$, as shown in Fig. 6. This structure can strengthen feature propagation and reuse features achieved from every layer. We use DenseNet121 to finish final detection of aortic dissection on our test set.

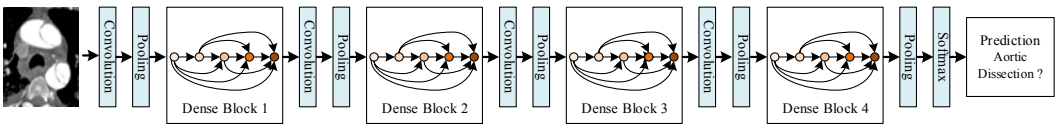

Figure 6: Structure of DenseNet121

4 Experimental results and analysis

The experiments are conducted with the Intel(R) Core (TM) i7-6500X CPU @ 2.50 GHz and 16.00 GB RAM. The Keras framework is applied for deep learning.

Our dataset organization is described in Section 2, which includes 4840 slice images coming from 88 CTA cases. The number and proportion of each class are listed in Tab. 1. 60% of the images are used for training, 20% are used for validation and 20% are used for test.

InceptionV3, ResNet50 and DenseNet121 are used for test and performance comparison. The

parameters for fine tuning are set the same for the three networks, which are listed in Tab. 2.

Table 2: Parameters for fine tuning

Batch Size	Epoch	Weight Decay	Momentum	Learning Rate
4	30	0.0001	0.9	0.001

Recall, *F*1-*score* and Matthews correlation coefficient (*MCC*) are used to evaluate our method, which are calculated as follows:

$$REC = \frac{TP}{TP + FN} \tag{13}$$

$$F1\_score = \frac{2 \times PRE \times REC}{PRE + REC} \tag{14}$$

$$\text{MCC} = \frac{TP \times TN - FP \times FN}{\sqrt{(TP + FP)(TP + FN)(TN + FP)(TN + FN)}} \tag{15}$$

where *TP* means the number of true positive, *FP* means the number of false positive, *FN* means the number of false negative and *TN* means the number of true negative. The comparison of InceptionV3, ResNet50 and DenseNet121 are shown in Fig. 7. It can be seen that DenseNet121 has the best performance of *Recall*, *F*1-*score* and *MCC*. It has far exceeded the performance of other method [Gayhart and Arisawa (2013)], which shew the sensitivity of 82.18%. But due to the difference of dataset and the ignorance of the aortic arch, the later method is not comparable with our method. Even though, our method still shows much better performance.

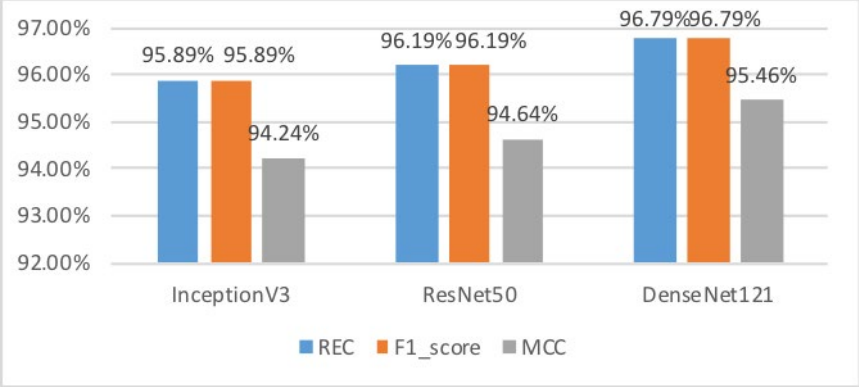

Figure 7: Evaluation comparison

In order to further investigate the difference of different networks, *REC*, *PRE* and *F*1_*score* for each category are further investigated. *PRE* is calculated by

$$PRE = \frac{TP}{TP + FP} \tag{16}$$

The results for each category are listed and compared in Tab. 3. It can be seen that ResNet50 shows best detection results for the CTA images of class 0, while DenseNet121 shows relative better detection results for the CTA images of Class 1, Class 2 and Class 3.

Table 3: Performance comparison for each class

		PRE	*REC*	*F*1_*score*
Class 0 (Normal aortic arch)	InceptionV3	0.96644	**0.97297**	0.96970
	ResNet50	**0.97959**	**0.97297**	**0.97627**
	DenseNet121	0.96622	0.96622	0.96622
Class 1 (Normal ascending and descending arch)	InceptionV3	0.91948	**0.98883**	0.95289
	ResNet50	0.93122	0.98324	0.95652
	DenseNet121	**0.94865**	0.98045	**0.96429**
Class 2 (Aortic arch with dissection)	InceptionV3	**0.99248**	0.96350	0.97778
	ResNet50	0.97122	**0.98540**	**0.97826**
	DenseNet121	0.97810	0.97810	0.97810
Class 3 (Ascending and descending arch with dissection)	InceptionV3	**0.98788**	0.92090	0.95322
	ResNet50	0.98498	0.92655	0.95488
	DenseNet121	0.98538	**0.95198**	**0.96839**

Since there are multiple categories in our dataset, the *macro* and *micro* average values are investigated to reflect the performance comprehensively, which are calculated as follows:

$$macro\_PRE = \frac{1}{n}\sum_{i=1}^{n} PRE_i \tag{17}$$

$$macro\_REC = \frac{1}{n}\sum_{i=1}^{n} REC_i \tag{18}$$

$$macro\_F1 = \frac{2 \times macro\_PRE \times macro\_REC}{macro\_PRE + macro\_REC} \tag{19}$$

$$micro\_PRE = \frac{\overline{TP}}{\overline{TP} \times \overline{FP}} \tag{20}$$

$$micro\_REC = \frac{\overline{TP}}{\overline{TP} \times \overline{FN}} \tag{21}$$

$$micro\_F1 = \frac{2 \times micro\_PRE \times micro\_REC}{micro\_PRE + micro\_REC} \tag{22}$$

Weighted average are further calculated by weighted the number of true instances for each category. The compressive results are shown in Tab. 4.

Table 4: Comprehensive Performance comparison

		PRE	*REC*	*F*1_*score*
micro Average	InceptionV3	0.95888	0.95888	0.95888
	ResNet50	0.96189	0.96189	0.96189
	DenseNet121	**0.96790**	**0.96790**	**0.96790**
macro Average	InceptionV3	0.96657	0.96155	0.96340
	ResNet50	0.96675	0.96704	0.96648
	DenseNet121	**0.96959**	**0.96919**	**0.96925**
Weighted Average	InceptionV3	0.96077	0.95888	0.95892
	ResNet50	0.96299	0.96189	0.96186
	DenseNet121	**0.96835**	**0.96790**	**0.96793**

From Tab. 4, it can be seen that DenseNet121 has best compressive performance than InceptionV3 and ResNet50.

5 Conclusions

In this work, we build a CTA image library with 88 CT cases, 43 cases of aortic dissection and 45 cases of health. An aortic dissection detection method based on CTA images is proposed. ROI is extracted based on binarization and morphology opening operation. The deep learning model DenseNet121 is applied after the preprocessing of the datasets. The accuracy and sensitivity are investigated. It is shown that deep learning methods can achieve much better performance than the traditional method. And among these deep learning methods, DenseNet121 can exceed other networks such as ResNet50 and InceptionV3. In the next step, we will try to increase the performance further and apply our method to the real application system.

Acknowledgment: This work is supported by the National Natural Science Foundation of China (No. 61772561), the National Natural Science Foundation of Hunan (No. 2019JJ50866), the Key Research & Development Plan of Hunan Province (No. 2018NK2012), the Postgraduate Science and Technology Innovation Foundation of Central South University of Forestry and Technology (No. 20183034).

Conflicts of Interest: The authors declare that they have no conflicts of interest to report regarding the present study.

References

Dehghan, E.; Wang, H.; Syeda-Mahmood, T. (2017): Automatic detection of aortic dissection in contrast-enhanced CT. *IEEE 14th International Symposium on Biomedical Imaging*, pp. 557-560.

Dou, Q.; Chen, H.; Yu, L.; Zhao, L.; Qin, J. et al. (2016): Automatic detection of cerebral microbleeds from MR images via 3D convolutional neural networks. *IEEE Transactions on Medical Imaging*, vol. 35, no. 5, pp. 1182-1195.

Gayhart, M.; Arisawa, H. (2013): Automated detection of healthy and diseased aortae from images obtained by contrast-enhanced CT scan. *Computational and Mathematical Methods in Medicine*, vol. 2013, no. 26, pp. 107871-107877.

He, K.; Zhang, X.; Ren, S.; Sun, J. (2015): Deep residual learning for image recognition. *IEEE Conference on Computer Vision and Pattern Recognition*, pp. 1-12.

Huang, G.; Liu, Z.; Maaten, L. V. D.; Weinberger, K. Q. (2017): Densely connected convolutional networks. *IEEE Conference on Computer Vision and Pattern Recognition*, pp. 1-9.

Ingle, P. D.; Kaur, P. (2017): Adaptive thresholding to robust image binarization for degraded document images. *1st International Conference on Intelligent Systems and Information Management*, pp. 189-193.

Kooi, T.; Litjens, G.; Van, G. B.; Gubern-Mérida, A.; Sánchez, C. I. et al. (2017): Large scale deep learning for computer aided detection of mammographic lesions. *Medical Image Analysis*, vol. 35, no. 24, pp. 303-312.

Li, H.; Qin, J. H.; Xiang, X. Y.; Ma, W. T.; Xiong, N. N. (2018): An efficient image matching algorithm based on adaptive threshold and RANSAC. *IEEE ACCESS*, vol. 6. pp. 66963-66697.

Moghaddam, R. F.; Cheriet, M. (2010): A multi-scale framework for adaptive binarization of degraded document images. *Pattern Recognition*, vol. 43, no. 6, pp. 2186-2198.

Najman, L.; Talbot, H. (2013): *Mathematical Morphology: From Theory to Applications.* ISTE, Wiley.

Otsu, N. (1979): A threshold selection method from gray-level histograms. *IEEE Transactions on Systems, Man, and Cybernetics*, vol. 9, no. 1, pp. 62-66.

Sirinukunwattana, K.; Raza, S. E. A; Tsang, Y. W.; Snead, D. R.; Cree, I. A. et al. (2016): Locality sensitive deep learning for detection and classification of nuclei in routine colon cancer histology images. *IEEE Transactions on Medical Imaging*, vol. 35, no. 5, pp. 1196-1206.

Szegedy, C.; Liu, W.; Jia, Y.; Sermanet, P.; Reed, S. et al. (2015): Going deeper with convolutions. *IEEE Conference on Computer Vision and Pattern Recognition*, pp. 1-9.

Szegedy, C.; Vanhoucke, V.; Ioffe, S.; Shlens, J.; Wojna, Z. (2016): Rethinking the inception architecture for computer vision. *IEEE Conference on Computer Vision and Pattern Recognition*, pp. 2818-2826.

Van Grinsven, M.; Van Ginneken, B.; Hoyng, C.; Theelen, T.; Sanchez, C. (2016): Fast convolutional neural network training using selective data sampling: application to

hemorrhage detection in color fundus images. *IEEE Transactions on Medical Imaging*, vol. 35, no. 5, pp. 1273-1284.

Zheng, M.; Carr, J. J.; Ge, Y. R. (2013): Automatic aorta detection in non-contrast 3D cardiac CT images using bayesian tracking method. *International MICCAI Workshop on Medical Computer Vision*, pp. 130-137.

Zreik, M.; Lessmann, N.; Hamersvelt, R. V.; Wolterinka, J. M.; Voskuilc, M. et al. (2018): Deep learning analysis of the myocardium in coronary CT angiography for identification of patients with functionally significant coronary artery stenosis. *Medical Image Analysis*, vol. 44, pp. 72-85.